Key Points:
- New data set of radiosonde observations over first year sea ice in the Arctic North Atlantic sector, from January to June 2015
- Rapid increases in column-integrated water vapor correspond to synoptic activity and track lower latitude air masses
- Tropospheric static stability is similar for N-ICE2015 and SHEBA, despite different location, sea ice thickness, and snow cover

Vertical thermodynamic structure of the troposphere during the Norwegian young sea ICE expedition (N-ICE2015)

Markus Kayser[1,2] (ID), Marion Maturilli[1] (ID), Robert M. Graham[1,3] (ID), Stephen R. Hudson[3] (ID), Annette Rinke[1] (ID), Lana Cohen[3] (ID), Joo-Hong Kim[4] (ID), Sang-Jong Park[4] (ID), Woosok Moon[5] (ID), and Mats A. Granskog[3] (ID)
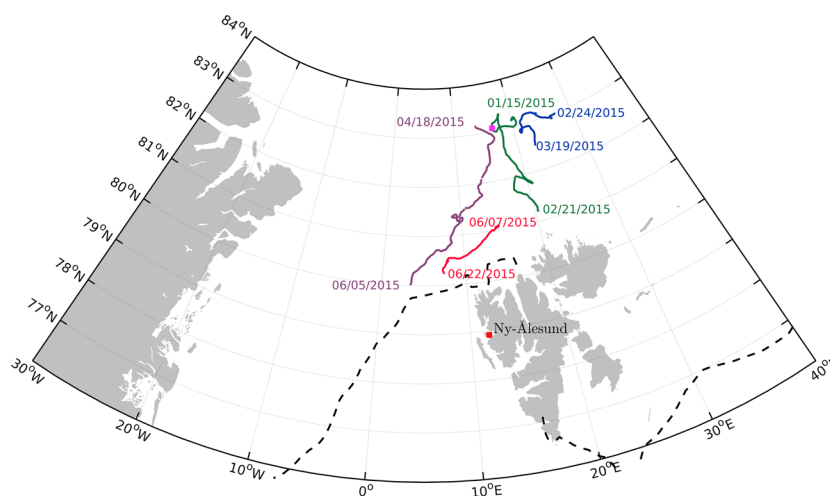
[1] Alfred Wegener Institute, Helmholtz Centre for Polar and Marine Research, Potsdam, Germany, [2] Institute of Physics and Astronomy, University of Potsdam, Potsdam, Germany, [3] Norwegian Polar Institute, Tromsø, Norway, [4] Korea Polar Research Institute, Incheon, South Korea, [5] Department of Applied Mathematics and Theoretical Physics, University of Cambridge, Cambridge, UK

Abstract The Norwegian young sea ICE (N-ICE2015) expedition was designed to investigate the atmosphere-snow-ice-ocean interactions in the young and thin sea ice regime north of Svalbard. Radiosondes were launched twice daily during the expedition from January to June 2015. Here we use these upper air measurements to study the multiple cyclonic events observed during N-ICE2015 with respect to changes in the vertical thermodynamic structure, moisture content, and boundary layer characteristics. We provide statistics of temperature inversion characteristics, static stability, and boundary layer extent. During winter, when radiative cooling is most effective, we find the strongest impact of synoptic cyclones. Changes to thermodynamic characteristics of the boundary layer are associated with transitions between the radiatively "clear" and "opaque" atmospheric states. In spring, radiative fluxes warm the surface leading to lifted temperature inversions and a statically unstable boundary layer. Further, we compare the N-ICE2015 static stability distributions to corresponding profiles from ERA-Interim reanalysis, from the closest land station in the Arctic North Atlantic sector, Ny-Ålesund, and to soundings from the SHEBA expedition (1997/1998). We find similar stability characteristics for N-ICE2015 and SHEBA throughout the troposphere, despite differences in location, sea ice thickness, and snow cover. For Ny-Ålesund, we observe similar characteristics above 1000 m, while the topography and ice-free fjord surrounding Ny-Ålesund generate great differences below. The long-term radiosonde record (1993–2014) from Ny-Ålesund indicates that during the N-ICE2015 spring period, temperatures were close to the climatological mean, while the lowest 3000 m were 1–3°C warmer than the climatology during winter.

Plain Language Summary The Norwegian young sea ICE (N-ICE2015) expedition was designed to investigate the atmosphere-snow-ice-ocean interactions in the young and thin sea ice regime north of Svalbard. Radiosondes were launched twice daily during the expedition from January to June 2015. Here we use these upper air measurements to study the multiple cyclonic events observed during N-ICE2015 with respect to changes in the vertical thermodynamic structure, moisture content, and the atmospheric boundary layer characteristics. During winter, we find the strongest impact of synoptic cyclones, which transport warm and moist air into the cold and dry Arctic atmosphere. In spring, incoming solar radiation warms the surface. This leads to very different thermodynamic conditions and higher moisture content, which reduces the contrast between stormy and calm periods. Further, we compare the N-ICE2015 measurements to corresponding profiles from ERA-Interim reanalysis, from the closest land station in the Arctic North Atlantic sector, Ny-Ålesund, and to soundings from the SHEBA expedition (1997/1998). We find similar stability characteristics for N-ICE2015 and SHEBA throughout the troposphere, despite differences in location, sea ice thickness, and snow cover. The comparisons highlight the value of the N-ICE2015 observation and show the importance of winter time observations in the Arctic North Atlantic sector.

1. Introduction

The increase in Arctic surface air temperature (SAT) from 1875 to 2008 has been twice that of the Northern Hemisphere [*Bekryaev et al.*, 2010]. Moreover, Arctic warming has accelerated by 0.6°C per decade in recent

Figure 1. Map of the Atlantic sector of the Arctic centering on the track of R/V *Lance* during ice drifts on the Floes 1–4 colored in green, blue, purple, and red, respectively. The magenta square marks ship position during the start of the major storm event on 3 February (M3). The location of Ny-Ålesund is marked by the red dot. The black dashed line shows the mean sea ice edge for January–June 2015 (from ERA-Interim reanalysis [*Dee et al.*, 2011]).

years (1981 to 2012) [*Comiso and Hall*, 2014]. The most visible manifestation of this "Arctic amplification" has been the diminishing sea ice extent and volume over the past decades [*Wang et al.*, 2012].

An interesting aspect of Arctic amplification is the enhanced warming of the atmospheric boundary layer (ABL) compared to the free troposphere [*Serreze and Barry*, 1988; *Screen and Simmonds*, 2010]. This warming is strongest during winter months, while the most rapid sea ice decline has been observed during the fall. *Graversen and Wang* [2009] showed, using model simulations with a fixed surface albedo, that amplified boundary layer warming occurs even in the absence of an ice-albedo feedback. This demonstrates that other processes such as water vapor and cloud feedbacks are important for explaining Arctic warming.

Surface atmosphere fluxes and the characteristics of the Arctic stable ABL over multiyear sea ice have been analyzed extensively using data from the 1997 t1998 Surface Heat Budget of the Arctic (SHEBA) drift expedition [*Uttal et al.*, 2002; *Rinke et al.*, 2004; *Shupe et al.*, 2006; *Grachev et al.*, 2007]. These data have been used to develop boundary layer parameterization schemes for climate models in the Arctic region [*Andreas et al.*, 2010; *Lüpkes and Gryanik*, 2015]. However, it is uncertain how representative the SHEBA data are for today's thinner sea ice regime, and how the decrease in sea ice thickness affects ABL characteristics in the Arctic.

SHEBA data show that synoptic activity drives Arctic winter conditions over sea ice into two distinct states, the radiative "clear state" and the "opaque state." [*Stramler et al.*, 2011; *Persson et al.*, 2016; *Graham et al.*, 2017]. Due to radiative cooling of the surface, the clear state is characterized by strong static stability developing under a deep surface-based temperature inversion (SBI) with large vertical extent [*Pithan and Mauritsen*, 2014; *Pithan et al.*, 2016]. Under these conditions the atmospheric mixed layer is shallow, with an extent less than 100 m. This results in the boundary layer and free troposphere becoming decoupled. The opaque state is characterized by cloudy conditions, likely including both cloud liquid water and ice, the absence of a temperature inversion at the surface, and strong downwelling longwave radiation. The resultant net radiation fluxes during opaque states is close to 0 W m^{-2} [*Stramler et al.*, 2011; *Graham et al.*, 2017].

New in situ measurements from the Arctic are vital, because reanalyses and satellite observations inadequately represent surface-based inversions under stable conditions [*Tjernström and Graversen*, 2009; *Liu et al.*, 2015]. The lack of in situ observations from this region, particularly during winter, has hindered model development. The SHEBA data have been used extensively for this, but most models and reanalyses fail to simulate the two Arctic winter states or boundary layer inversions accurately [*Engström et al.*, 2014; *Pithan et al.*, 2016; *Graham et al.*, 2017].

The Norwegian young sea ICE (N-ICE2015) expedition took place from January to June 2015 [*Granskog et al.*, 2016], in the pack ice north of the Svalbard archipelago (Figure 1). During this time, the ship R/V *Lance* conducted four ice drifts, referred to as Floes 1–4 [*Cohen et al.*, 2017]. N-ICE2015 applied a multidisciplinary

approach and obtained simultaneous atmospheric, oceanographic, sea ice, snow cover, and biochemical observations, during each drift leg. The purpose of the campaign was to investigate the effect of a thinner Arctic sea ice pack on atmosphere-snow-ice-ocean-ecosystem interactions and thus to forward our understanding of the response of the Arctic climate system to the ongoing warming.

In this study, we present a new radiosonde data set from the Atlantic sector of the Arctic Ocean that covers Arctic conditions of winter, spring, and early summer during N-ICE2015. We discuss changes in the atmospheric structure, moisture content, stability, and ABL height during the numerous cyclonic events observed [*Cohen et al.*, 2017; *Graham et al.*, 2017]. We further derive statistics of temperature inversion characteristics from the radiosonde data set. Finally, we compare seasonal mean distributions of static stability and seasonal mean temperature profiles for the N-ICE2015 data [*Hudson et al.*, 2017] with radiosonde records from Ny-Ålesund station [*Maturilli and Kayser*, 2016], with radiosoundings obtained during the SHEBA ice drift expedition (1997/1998) [*Uttal et al.*, 2002], as well as with ERA-Interim reanalysis data [*Dee et al.*, 2011].

2. Data Description

During the N-ICE2015 expedition, radiosondes were launched twice per day. The radiosondes measured air temperature, pressure, relative humidity, wind speed, and direction during their balloon-borne ascent to altitudes of about 30 km. In accordance with World Meteorological Organization (WMO) standards, sondes were released around 11 and 23 UTC to complete the tropospheric ascent at 12 and 00 UTC.

The N-ICE2015 radiosonde data were transmitted to the World Meteorological Organization-Global Telecommunication System (WMO-GTS) to contribute to meteorological forecast models and climate reanalyses, e.g., ERA-Interim [*Dee et al.*, 2011]. Throughout Floe 1 (Figure 1), sondes were prepared and released from the sea ice beside R/V *Lance*. At all other times, sondes were prepared and released from the main deck of R/V *Lance*. This was located approximately 3 m above sea level. Due to the movement of the ship during each of the four different drift phases, Floes 1 to 4, the radiosondes were launched from different geographic positions (Figure 1).

The Vaisala RS92-SGP radiosondes, launched during N-ICE2015 [*Hudson et al.*, 2017], have a data sampling rate of 2 s. These measure pressure, temperature, and relative humidity directly. Wind speed, wind direction, and geopotential height are retrieved based on GPS. Uncertainties, accuracies, and ranges of the individual sensors for the RS92-SGP are stated in the manufacturer's technical information sheet (www.vaisala.com).

Overall, the N-ICE2015 expedition can be split into two nearly continuous periods. These correspond to a winter period (January to March), during drift of Floes 1 and 2, and spring period over sea ice (April to June), during drift of Floes 3 and 4, respectively. Data gaps in the radiosonde record during these periods were related to severe weather conditions, not allowing for radiosonde launches, ice floe breakup, and repositioning of the ship, and to a scheduled pause in the course of the campaign, between Floes 2 and 3. These upper air observations from N-ICE2015 upper air data provide a valuable opportunity to analyze the vertical structure of atmospheric processes over the Arctic ice-ocean environment.

To place the N-ICE2015 upper air observations into a climatological context, we consider the long-term radiosonde data record from the nearby land station Ny-Ålesund (78.9°N, 11.9°E), which is located on the west coast of Spitsbergen (Figure 1). N-ICE2015 and Ny-Ålesund were typically separated by a distance between 150 and 500 km. The N-ICE2015 position during each sea ice drift was generally north of Svalbard (Figure 1). While the two sites are in close proximity, the underlying surfaces are distinctively different. N-ICE2015 is characterized by relatively level sea ice and some open-ocean leads. In contrast, Ny-Ålesund is characterized by snow on solid terrain with 800 m high mountains surrounding a mostly ice-free fjord.

Radiosondes have been launched on a daily basis at Ny-Ålesund, from 1993 to present, providing a homogenized radiosonde data set, [*Maturilli and Kayser*, 2016]. The same Vaisala RS92-SGP radiosondes that were launched during N-ICE2015 are used in Ny-Ålesund. Ny-Ålesund contributes to the Global Climate Observing System (GCOS) [*Dirksen et al.*, 2014] Upper Air Network (GRUAN), and so we use the GRUAN processed data here for our analyses. Differences between the manufacturer's (used for N-ICE2015) and the GRUAN processing have no influence on our analyses. Processing methods and uncertainties are documented by *Dirksen et al.* [2014].

The SHEBA expedition (1997/1998), discussed further in section 4, utilized Vaisala RS80 radiosondes [*Moritz*, 2007]. This radiosonde type suffered from several humidity biases [*Miloshevich et al.*, 2001]. A bias in temperature exists as well, but only for high altitudes ($p < 100$ hPa) [*Steinbrecht et al.*, 2008]. Therefore, we did not correct for biases in the analyses. We chose to compare distributions of tropospheric, static stability to minimize the effect of potentially biased measurements.

3. Upper Air Observations During N-ICE2015
3.1. Tropospheric Conditions

An overview of the tropospheric temperature above the N-ICE2015 location is given in Figure 2a, which displays the radiosonde temperature profiles for the entire N-ICE2015 expedition, covering polar night and polar day conditions. The transition between polar night and day occurred during the campaign break in April, marked by a large data gap. Generally, the mean temperature in the tropospheric column increases from the beginning until the end of the campaign, as is expected from the annual cycle. Toward the end of the campaign, during Floes 3 and 4, the ice camp was in proximity to the sea ice edge. On 25 May, the N-ICE2015 expedition drifted into warmer waters [*Meyer et al.*, 2017], and lower tropospheric temperatures exceeding 0°C were first seen on 1 June [*Cohen et al.*, 2017], marked by near-constant 0°C 2 m temperatures. Thus, the increase in air temperature was driven not only by increased shortwave flux but also by the proximity of the warm Atlantic Ocean (Figure 1).
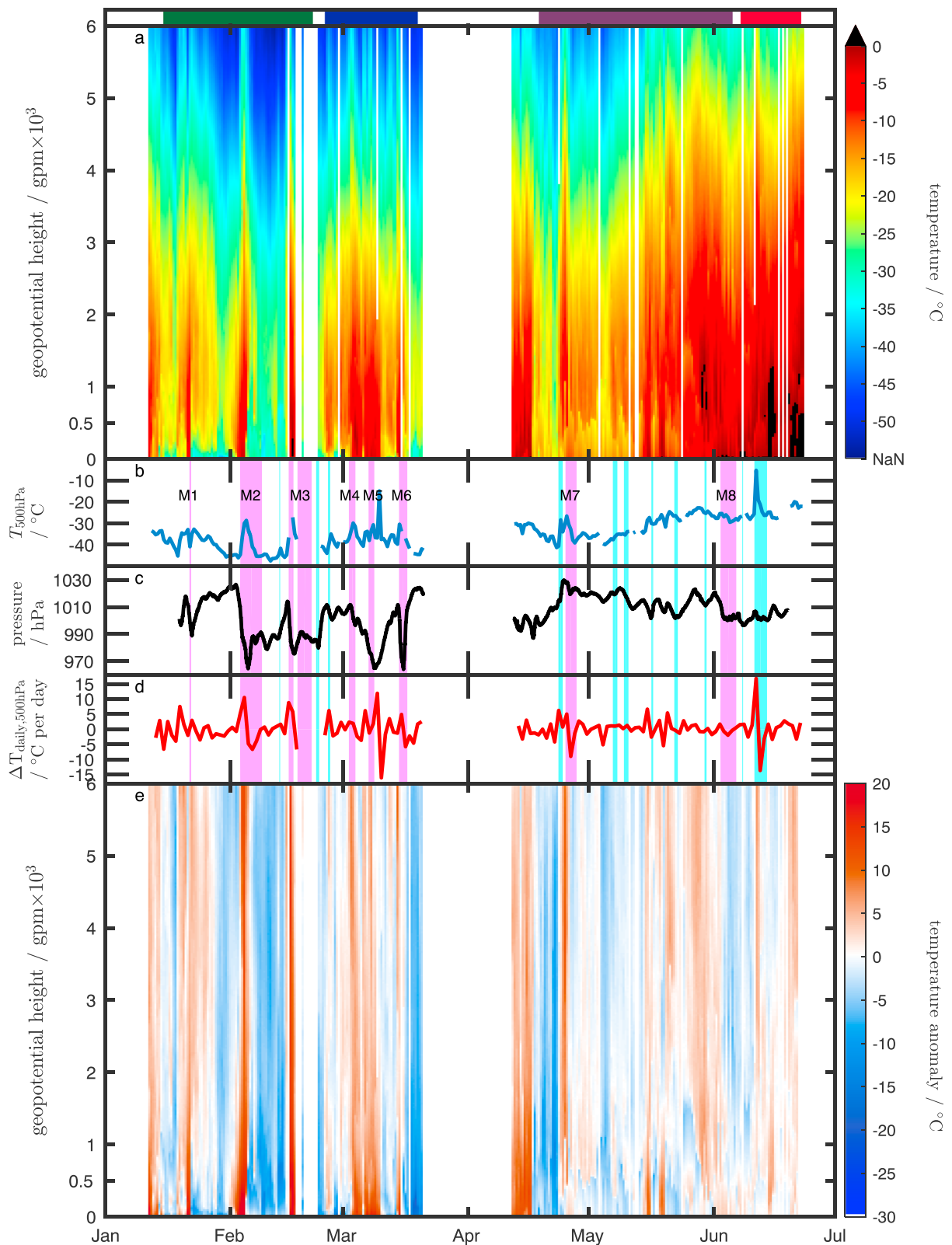
During the N-ICE2015 winter (Floes 1 and 2), there are frequent and large temperature fluctuations in the lower and middle troposphere (Figure 2b). These fluctuations result in changes from surface-based inversion layers with top temperatures below −20°C to deep surface-based nearly isothermal layers near but below 0°C. These changes are due to warm air advection associated with storm events. The N-ICE2015 winter period was marked by storm events that are described in detail by *Cohen et al.* [2017]. *Cohen et al.* [2017] identified six major (M1–M6) and three minor (m1–m3) storm events during the N-ICE2015 winter, defined by persistent high wind speeds and pressure drops in the surface meteorological observations [*Hudson et al.*, 2015]. These storms transported warm air masses from the open ocean into the sea ice region north of Svalbard. During these winter storms, the temperature rises throughout the entire tropospheric column and can lead to large temperature fluctuations on daily time scales (Figure 2b). For example, a temperature increase of ∼10°C in 24 h is observed at 500 hPa during the major storm events M2 and M3 (Figure 2d). Air temperatures even exceeded 0°C in the lowermost troposphere during one of the major storm events, 17 February at 0 UTC, before the termination of Floe 1. Shorter periods of temperature increase in the free troposphere are also observed during winter, and these are related to the three minor storm events, on 13, 22, and 25 February (Figure 2).

Calm periods between winter storm events during N-ICE2015 are associated with high-pressure conditions [*Graham et al.*, 2017] (Figure 10c). This enables strong surface radiative cooling, characteristic of the Arctic winter, that helps create a near-surface or surface-based inversion (Figure 2a). Consequently, temperature in the lower free troposphere up to 5 km altitude is generally higher than in the ABL. Such radiatively induced temperature inversions act to decouple mixed layer and the free troposphere and reduce mixing [*Andreas et al.*, 2000].

The spring period of N-ICE2015 (Floes 3 and 4) was characterized by less temperature variability and weaker temperature inversions compared to the winter period. The decreasing temperature variability during the N-ICE2015 from winter through spring and early summer is demonstrated by the temperature change over 24 h at the 500 hPa level (Figure 2d). Cyclone events during spring lead to 500 hPa temperature differences over 24 h between 2 and 5°C, compared with 5 to 10°C during winter. Polar day radiation conditions and the eventual melting of snow at the surface become gradually more important during the spring and early summer. Incoming radiative fluxes act to warm the surface and enhance mixing in the lowermost troposphere, and thereby the decoupling of the boundary layer is reduced [*Walden et al.*, 2017].
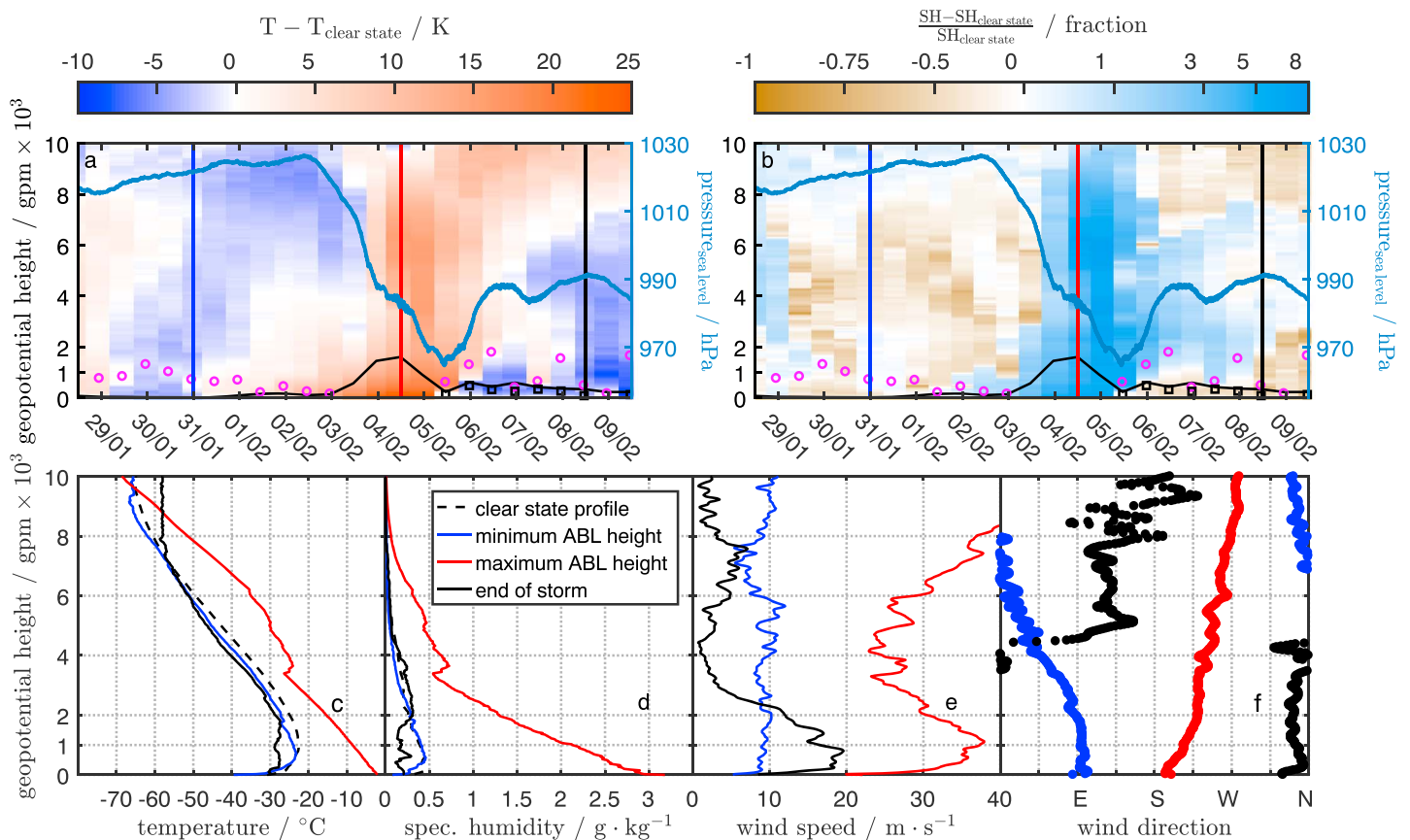
To remove the influence of the seasonal cycle and the changing ship position, we subtract a 21 day running mean from the N-ICE2015 radiosonde temperature profiles. The resulting temperature anomalies highlight the impact and influence of cyclones observed during N-ICE2015 (Figure 2e).

The onset of cyclonic events correlates with positive temperature anomalies (Figure 2e). This correlation is strongest during winter, where the positive temperature anomalies extend throughout the troposphere. Each storm event during the N-ICE2015 winter consists of an initial rapid warming with positive anomalies

Figure 2. Time-height cross section (a) of tropospheric temperature and (e) of tropospheric temperature anomaly, between observations and 21 day running mean, from radiosondes launched during the N-ICE2015 expedition, with major (M1 to M8) and minor storm events (magenta and cyan lines in Figures 2b–2d, respectively) as identified by *Cohen et al.* [2017] as well as (b) the 500 hPa temperature, (c) the pressure from R/V *Lance*'s ship sensor, and (d) the 500 hPa temperature change in 24 h. The drift of Floes' 1–4 (green, blue, purple, and red, respectively) are shown at the top.

Figure 3. Case study of the M2 storm event (on 3 February 2015) using the N-ICE2015 radiosonde data: Surface pressure from the R/V *Lance* ship sensor (blue line) and time-height cross sections of (a) temperature anomaly $\left(T - T_{clear}\right)$ and of (b) normalized specific humidity anomaly $\left(\frac{SH - SH_{clear}}{SH_{clear}}\right)$, the boundary layer height calculated from bulk Richardson number $\left(Ri_{crit} = 0.25\right)$ (black line), inversion top (magenta circles), and inversion base height (black squares). The soundings from 31 January 00 UTC (blue), 4 February 12 UTC (red), and 8 February 12 UTC (black) are marked with vertical lines; their corresponding (c) temperature, (d) specific humidity, (e) wind speed, and (f) wind direction profiles are shown in the lower panels.
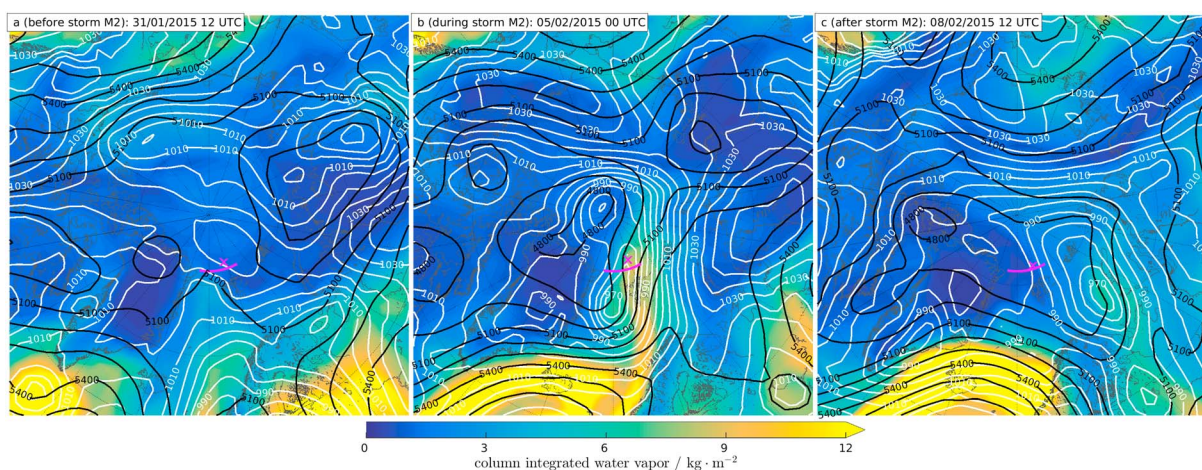
of about 15°C, followed by an abrupt cooling indicating the passage of a cold front. The strong cooling in the cold-air sector has magnitudes ranging from −8°C in the free troposphere to −20°C in the boundary layer. The radiosonde profiles show the cold front passing first near the surface and then at the progressively higher levels over time.

During spring, the correlation between the onset of storms and positive temperature anomalies holds, but the magnitudes are smaller than in winter (Figure 2e). In late May and June, anomalies in the lowermost troposphere are almost uniform. This shows that during late spring and early summer, temperature observations in the boundary layer are not as good an indicator of synoptic activity, since surface temperatures are always near the melting point. We observe positive tropospheric temperature anomalies associated with warm air advection during spring storms ranging from 5°C to 10°C, and negative temperature anomalies between −8°C and −1°C associated with cold-air advection (Figures 2d and 2e).

3.2. Case Study of an Extreme Cyclone Event

As a case study, we look at the 3 February major storm event (M2) [*Cohen et al.*, 2017, Figure 9] and its impact on moisture, atmospheric temperature, and atmospheric stability. This event represents the best example of a perturbation to the stable Arctic winter atmosphere during the N-ICE2015 expedition. This storm occurred after an extended calm period and was followed by a further calm and exceptionally cold period for this campaign (Figure 2). Additionally, the complete set of 12-hourly radiosonde data provides optimum data coverage.

The M2 storm can be interpreted as a perturbation from the radiatively clear atmospheric winter state [*Stramler et al.*, 2011; *Graham et al.*, 2017]. We average all winter (JFM) radiosondes launched under clear state

Figure 4. Polar stereographic projection showing mean sea level pressure (white contours), 500 hPa geopotential height (black contours), and total column water vapor (shaded contours) from (a) before, (b) during, and (c) after the M2 storm event, using ERA-Interim reanalysis in 2° × 2° resolution [*Dee et al.*, 2011]. The ship position and the cross section used in Figure 5 are marked by the magenta cross and line, respectively.

conditions to calculate the mean background state of the atmosphere (dashed line in Figures 3c and 3d). Radiative clear soundings are defined by averaging the surface net radiation 1 h prior to and after the radiosonde launch and selecting only the profiles with mean net radiation less than $-30\,W\,m^{-2}$ [*Stramler et al.*, 2011; *Graham et al.*, 2017].
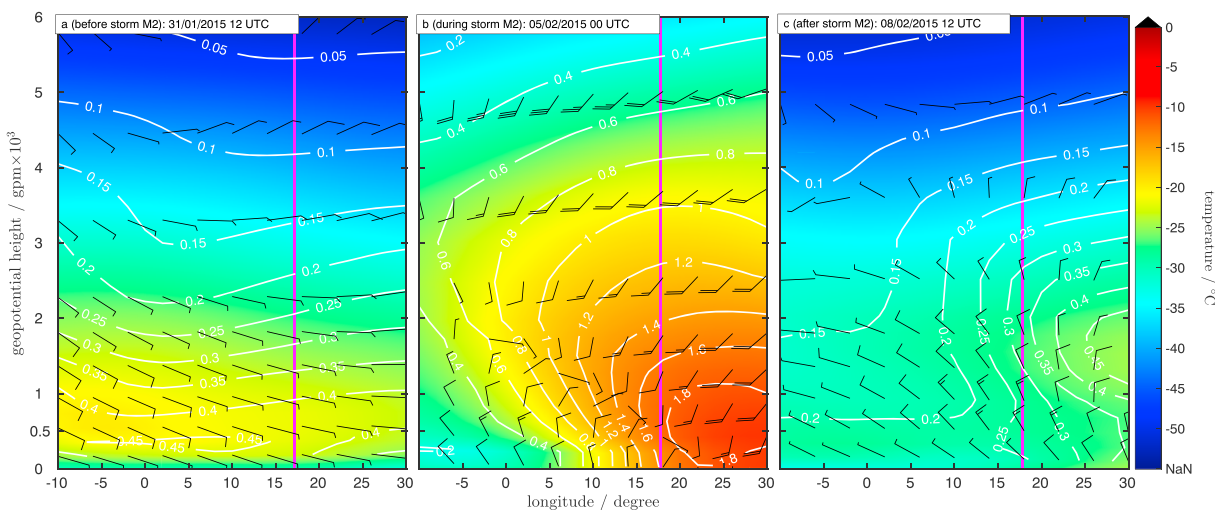
To investigate the impact of the M2 storm at the N-ICE2015 location, we compare the background radiatively clear atmosphere to the temperature and specific humidity profiles to those prior to the storm on 31 January at 0 UTC, when ABL height was at a minimum, during maximum storm intensity on 4 February at 12 UTC, when ABL height was at a maximum, and close to the end of the storm on 8 February at 12 UTC. These times are defined as when the ABL height is at its minimum on 31 January at 0 UTC, the ABL height maximum on 4 February at 12 UTC, and at the end of the storm on 8 February at 12 UTC. Over the course of the M2 storm, large quantities of snowfall occurred [*Cohen et al.*, 2017; *Merkouriadi et al.*, 2017]. Further, the distance to the ice edge was reduced markedly, starting from ca. 160 km on 31 January, decreasing to ca. 100 km on 5 February and increasing again to ~130 km on 8 February [Figure 2; *Itkin et al.*, 2017]. To relate the in situ measurements to the synoptic scale, we present contour maps and longitude-height cross sections from ERA-Interim reanalysis data for before (31 January 12 UTC), during (5 February 0 UTC), and after (8 February 12 UTC) the M2 storm (Figures 4 and 5).

Before the storm, low values of integrated water vapor (IWV) occur together with northeasterly winds, which advect cold polar air over the sea ice surface toward the N-ICE2015 location (Figures 4a and 5a). The in situ vertical temperature profile during this time shows low temperatures near the surface and a surface-based inversion (Figure 3c). The temperature difference to the background clear state profile is uniformly negative throughout the troposphere (Figure 3a), while the specific humidity content along the transect is low and agrees closely with the radiative clear state profile (Figures 5a and 3d).

At this time, the reanalyses shows a deepening low-pressure system in the Labrador Sea. This low-pressure system moved across Greenland into the Arctic North Atlantic sector and enabled warm and moist air from the Atlantic to enter the Arctic (Figures 4a and 4b).
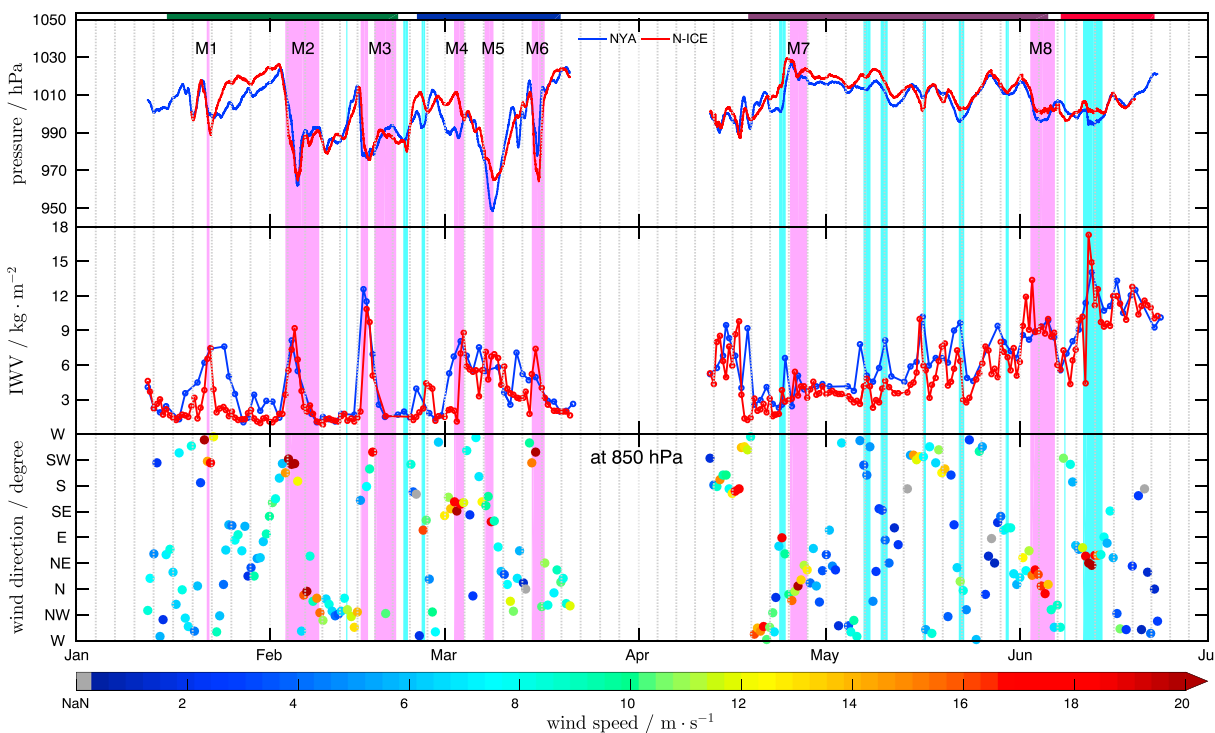
Over the course of the 4 days prior to the storm, the wind direction changes from east to south. During this time, wind speeds range from 5 to 9 m s^{-1} (Figures 5 and 6, bottom) and the inversion depth and strength decrease. This is indicated by vanishing temperature differences in the midtroposphere and the stronger warming near the ABL height, which remains below 200 m. Similar patterns are seen in the humidity anomalies (Figure 3b). Temperature anomalies within the ABL becomes positive 2 days prior to the storm event.

The maximum ABL height of 1600 m is reached on 4 February (Figure 3a), 1.5 days after the storm's onset. The maximum boundary layer height is accompanied by high wind speeds of over 20 m s^{-1} from southwest at 850 hPa (Figures 3e, 3f, and 5b). Warming throughout the entire tropospheric column and also peaks on 4 February at 12 UTC, with a maximum anomaly of ~28 K near the surface. Despite the strong wind-driven

Figure 5. Longitude-height cross section, as shown in Figure 4, presenting specific humidity in g kg^{-1} (white contours), horizontal wind speed in m s^{-1}, and direction in degrees (wind barbs with vane pointing in wind direction), and temperature (shaded contours) from (a) before, (b) during, and (c) after the M2 storm event, using ERA-Interim reanalysis in 2° × 2° resolution [*Dee et al.*, 2011]. The ship's longitude position is marked by the magenta line.

mixing and large boundary layer height, there is still an inversion present with base height around 3400 m (Figure 3c). Twelve hours later, a cold front slides underneath the warm air at the N-ICE2015 location accompanied by slower northerly winds. Temperature and specific humidity inversions quickly develop with a base close to the ABL height (Figures 5c and 3). The temperatures near the surface remain higher than the 31 January profile. The colocated temperature and humidity inversion likely indicates a cloud top inversion.

Figure 6. Time series during the N-ICE2015 expedition period including observations from AWIPEV research base in Ny-Ålesund: (top) Surface pressure from the R/V *Lance* ship sensor and AWIPEV weather station; (middle) integrated water vapor from radiosonde profiles at Ny-Ålesund and N-ICE2015; (bottom) wind direction and speed (color coded) at 850 hPa from N-ICE2015 radiosondes. Major (magenta) and minor (cyan) storm events as identified by *Cohen et al.* [2017] are indicated with vertical bars. The periods of ice camps for Floes 1–4 (green, blue, purple, and red) are shown at the top.

Temperature and humidity differences remain positive in the troposphere until 6 February at 12 UTC with decreasing anomaly magnitude. Even though the inversion recovers fast, near-surface temperatures remain about 3 K above precyclone conditions at the end of the event on 8 February. The impact on specific humidity does not outlast the storm period, as shown in the in situ reanalysis profiles for 8 February in Figures 3d and 5c, and in accordance with the distribution of IWV in the sector (Figures 3d, 4c, and 5c).

Woods and Caballero [2016] studied the temporal evolution of moisture intrusions, using composites of all intrusion events identified in ERA-Interim reanalyses during the months October to January 1990–2012. Similar to what we have shown for the M2 storm case study, they found that moisture intrusions affect the vertical structure of humidity and temperature 3–4 days prior to the event. Similarly, they also found that surface temperatures need more time to recover even after the inversion has reformed (Figures 3 and 5). Hence, the impact of synoptic cyclones on Arctic conditions lasts longer than the time span of the initial cyclone. *Woods and Caballero* [2016] found that peak warming at the inversion occurs about 12 h earlier than at the surface. However, in the chosen case study, peak warming is reached simultaneously at the surface and at the inversion level.
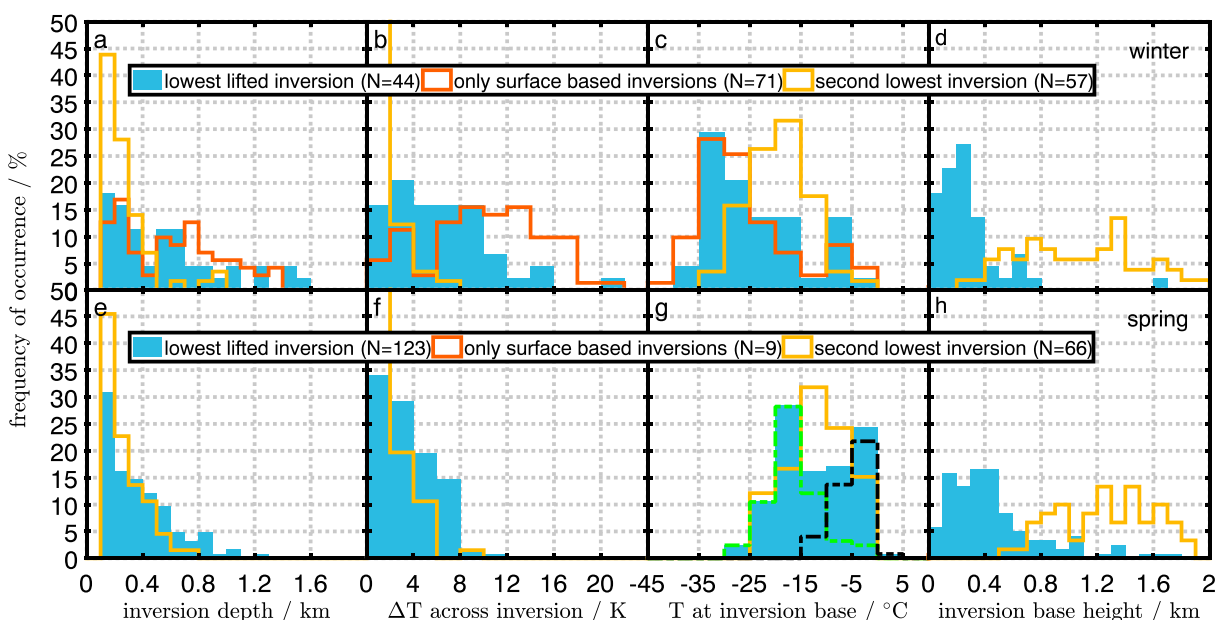
Analyzing individual case studies provides a view of the temporal development of the synoptic influence. Specifically, this analysis shows the change at the inversion level and the stages of ABL warming that occur during the transition from clear to opaque state (Figure 3). In this case study, the warming of the ABL prior to the storm is induced by the lowering of the temperature inversion top. This reduces the inversion extent and enables mixing of warm air aloft into the colder ABL [*Walden et al.*, 2017]. Such processes are also influenced by the presence of clouds and therefore differ from case to case.

3.3. General Cyclone Characteristics During N-ICE2015

R/V *Lance* was positioned along one of the main North Atlantic storm tracks toward the Arctic [*Serreze and Barry*, 1988]. Most synoptic storm events during the N-ICE2015 winter originated in the Greenland and Norwegian Seas. These storms passed directly over Ny-Ålesund and later N-ICE2015 on route to the central Arctic [*Cohen et al.*, 2017] [*Cohen et al.*, 2017, Figure 9] (see Figures S1 and S2 in the supporting information for time-height cross sections of Ny-Ålesunds temperature profiles and temperature anomalies from radiosoundings). In contrast with these winter storms, most of the spring synoptic cyclones during N-ICE2015 were centered over the Barents and Kara Seas [*Cohen et al.*, 2017, Figure 10]. Hence, during spring cyclones, Ny-Ålesund and N-ICE2015 were at approximately the same distance to the low-pressure centers.

The N-ICE2015 storm events, as identified from wind speed increases and pressure drops by *Cohen et al.* [2017], correspond to surface pressure drops, increases in IWV, and changes in wind speed and direction at both N-ICE2015 and Ny-Ålesund (Figure 6). In winter, the variations in surface pressure are large due to passing cyclones, with a minimum absolute value of 948 hPa observed at Ny-Ålesund on 8 March, and three pressure drops below 970 hPa at the N-ICE2015 site. During spring, surface pressure variations are smaller with minimum values remaining above 990 hPa (Figure 6). Surface pressure values under high-pressure influence during both campaign phases ranged from 1020 to 1030 hPa. The larger pressure variability observed during winter can be explained by the cyclone passing directly over the observation sites, while in spring the cyclone centers were located farther away [*Cohen et al.*, 2017], and winter cyclones are generally more intense than during spring/summer [*Serreze et al.*, 1997].

Storm events in the Arctic are expected to advect warm and moist air to the observation site [*Woods and Caballero*, 2016]. During winter, cyclone events cause a large change in IWV: The values fluctuate around 2 kg m^{-2} in the absence of synoptic storms and are 2 to 4 times higher under a storm's impact. For example, during the extreme cyclone event M3 the IWV is ∼11 kg m^{-2} for N-ICE2015 and ∼13 kg m^{-2} for Ny-Ålesund (Figure 6, middle). These high values of IWV are associated with southerly to southwesterly winds. Sudden moisture increases and decreases are intricately tied to the direction of air mass advection [*Woods and Caballero*, 2016]. Indicative of the advection is the wind direction measured at 850 hPa by the N-ICE2015 radiosondes, see Figure 6 (bottom). The moisture impact of winter storms occurs 0.5 to 1 day earlier at Ny-Ålesund with respect to N-ICE2015. The temperature anomalies (Figure 2) show that peak moisture increases and southerly winds with wind speeds above 14 m s^{-1} (Figures 6, middle and 6, bottom) coincide with the warm front passage at the N-ICE2015 position. When the cold front arrives, pressure increases, IWV rapidly decreases, and the wind abruptly turns toward north, with wind speeds remaining high. During calm

Figure 7. (a–h) Red lines show distributions of surface-based inversions; blue patches show distributions for a first but lifted inversion with base below 3000 m, when no surface inversion was present; yellow lines show distributions for the second lowest inversion layer with base below 3000 m, when present above either a surface-based or surface-lifted inversion; the green and black dashed lines refer to early (73 soundings) and late (55 soundings) spring, before and after 24 May 2015, respectively.

periods in winter, the 850 hPa wind speeds are generally in the range from 2 to 10 m s^{-1} from northwesterly to northeasterly directions. Both IWV and wind observations are in agreement with the advection along the cyclone track described in *Cohen et al.* [2017].

During spring the overall moisture path rises continuously, starting from ∼3 kg m^{-2} in April to ∼12 kg m^{-2} in late June (Figure 6). Cyclones still cause a sudden increase in IWV. In the later period of the expedition (Floes 3 and 4), the peak moisture events occur under zonal wind influence [*Cohen et al.*, 2017], and the IWV maxima occur at both sites almost simultaneously. Only during the second half of May and in June, moisture peaks are observed first at the N-ICE2015 location, associated with strong northeasterly winds. As an example, we show the minor storm (m10) [*Cohen et al.*, 2017], starting on 11 June, to discuss the radiosonde observations in connection with the synoptic conditions in spring [*Cohen et al.*, 2017]. Two days prior to m10, southerly winds advect air across the Svalbard archipelago toward Ny-Ålesund and the N-ICE2015 site (Figure 1) leading to a small increase in IWV of ∼9 kg m^{-2}. After a change to northeasterly winds with high wind speeds around 20 m s^{-1} the IWV increases to more than 17 kg m^{-2} (Figure 6). By that time, ERA-Interim reanalysis shows that a low-pressure system was situated with its center southeast of Svalbard in the Kara Sea (not shown), which drove advection of moist air from the open ocean in the Kara Sea.

We conclude that the observed increases in IWV during the N-ICE2015 expedition are related to synoptic-scale cyclones, associated with moist air masses advected from lower latitudes. *Cohen et al.* [2017] show that most winter cyclones passed directly over the N-ICE2015 site (Floes 1 and 2) and that most of the spring cyclones (Floes 3 and 4) intensified over the Barents and Kara Seas, before the air mass reached Svalbard and the N-ICE2015 site. These findings imply that the relative change in IWV is a good indicator for cyclonic activity in the Arctic sea ice region and an indicator for lower latitude air masses (Figure 4).

3.4. Temperature Inversions and Stability During N-ICE2015

Here we present basic characteristics of the winter and spring temperature inversions for N-ICE2015. We classify the inversions as either surface-based inversion (SBI) or lowest inversion located above the surface (LI), and second inversions (SI). We exclude inversions with base heights greater than 3000 m (Figure 7). We analyze the 247 soundings with inversions starting below 3000 m (115 out of 122 for winter and 132 out of 136 for spring). For the definition of temperature inversions we follow *Andreas et al.* [2000]: with thresholds for minimum depth and temperature difference between two consecutive data points of 100 m and 0.3 K, respectively.

The evolution of static stability during the N-ICE2015 expedition is determined from virtual potential temperature according to *Stull* [1991] (and also *Wallace and Hobbs* [2006]) (Figure 8). This nonlocal method has the advantage of accounting for the local lapse rate and air parcel movement alike and thus accounts for vertical fluxes and mixing across finite distances in the boundary layer and above. However, distinguishing between weakly stable and neutral regions is difficult and depends on the profile's vertical resolution. Therefore, we also present frequency distributions of the vertical gradient of virtual potential temperature, $\partial\Theta_v/\partial z$, to emphasize seasonal differences in stability (Figures 9a and 9e).

We further calculate ABL height using a bulk Richardson approach [*Hanna*, 1969] (see supporting information). This requires vertical profiles of temperature, pressure, and wind as outlined by *Zhang et al.* [2014]. The ABL height is defined as the first height exceeding a critical Richardson number, typically $0.5 > Ri_{crit} > 0.25$ [*Taylor*, 1931; *Gryning and Batchvarova*, 2002; *Zilitinkevich and Baklanov*, 2002; *Zhang et al.*, 2014]. Here we follow the recommendation by *Zhang et al.* [2014] who proposed $Ri_{crit} = 0.25$ based on SHEBA data. This method does not incorporate surface fluxes and therefore implies that the boundary layer is in steady state and results in an equilibrium ABL height rather than in an instantaneous height [*Zilitinkevich and Baklanov*, 2002].

3.4.1. Winter

During the N-ICE2015 winter (Floes 1 and 2), a temperature inversion was present in 94% of 122 soundings, and 58% of the total winter profiles show a surface-based inversion. Surface observations from the 10 m meteorological tower show a higher occurrence of SBIs (approximately 80%) compared with the radiosonde data [*Cohen et al.*, 2017]. The lowermost 10 m of the atmosphere are not resolved by the radiosonde measurements used here. LIs are found in 36% of the radiosonde soundings (Figures 7a–7d). Including SBIs, 95% of the winter inversions have a base below 500 m. Temperature inversions with bases above 3000 m are associated to the frontal zone of cyclonic events, such as in the case study of storm M2 (section 3).
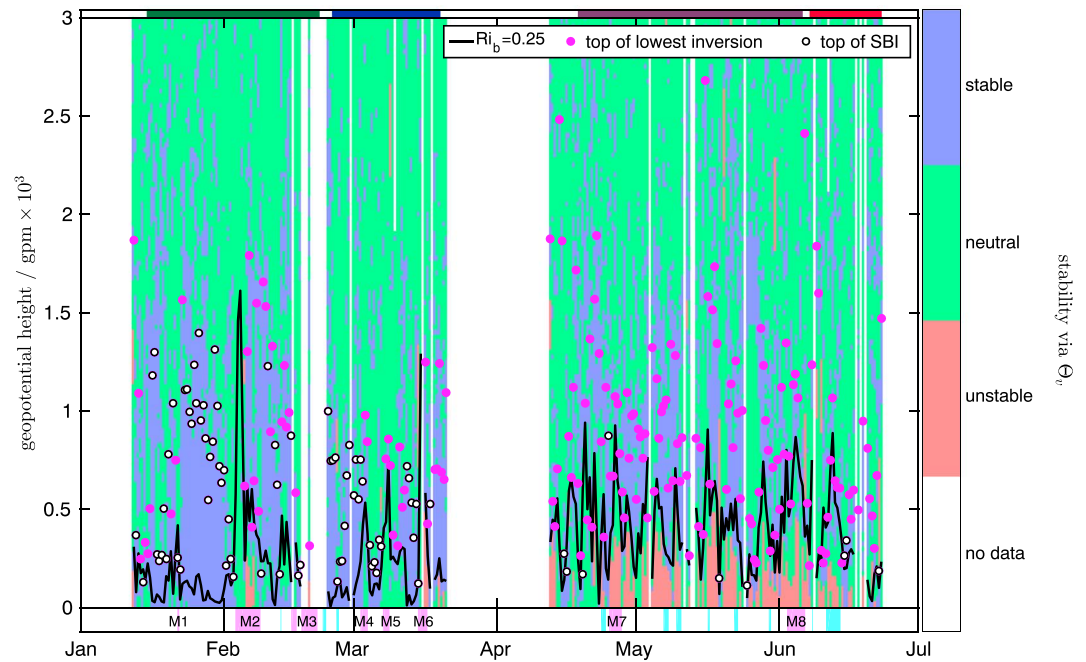
For winter, Figure 7 shows that LIs and SBIs have the same bimodal distribution of temperature at inversion base with peaks corresponding to the radiatively clear state and the opaque state, respectively [*Graham et al.*, 2017]. SBIs and LIs differ in the observed temperature change across the inversion (Figure 7b). But the inversion depth distributions indicate only a slightly higher frequency of occurrence of vertical extents larger than 700 m for SBIs than for LIs (Figure 7a). Hence, Figures 7a and 7b indicate that the temperature gradient across a SBI is larger than across a LI.

SIs are characteristic in the N-ICE2015 radiosoundings. These are present in 50% of the inversion cases. Of the SIs, 47% occurs with a vertical extent of between 100 and 400 m, and with temperature changes smaller than 4 K (Figures 7a and 7b). In contrast to LIs, SIs have a monomodal rather than bimodal base temperature distribution, and their base height can be found over a broader range (Figures 7c and 7d).
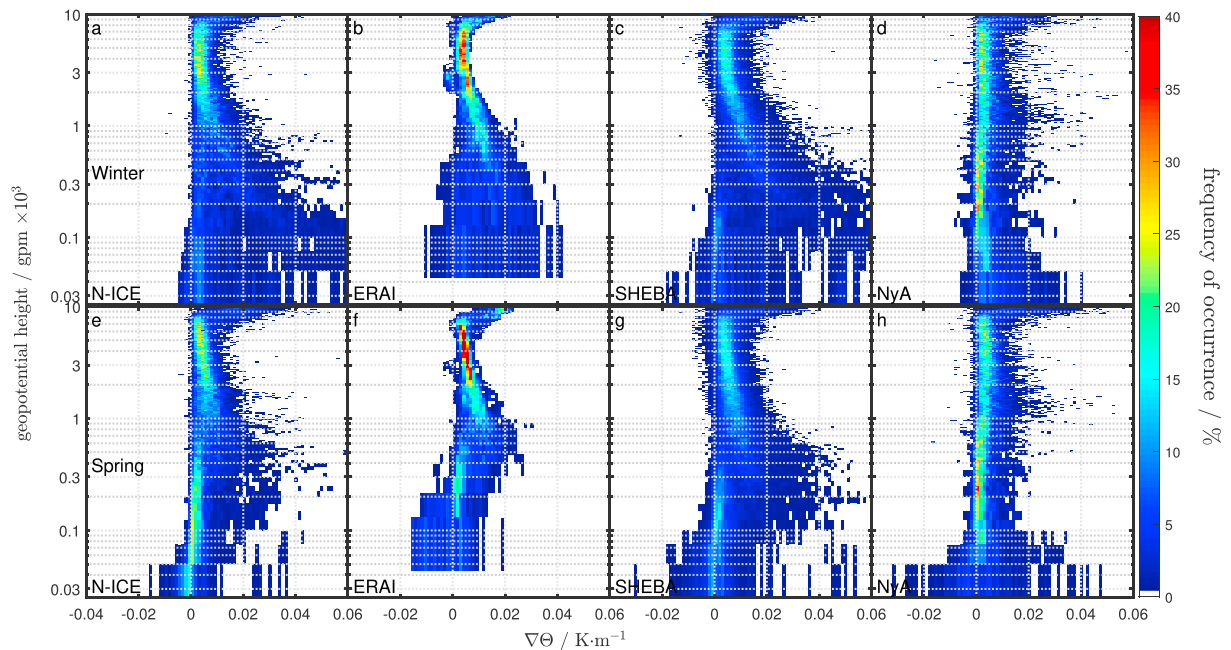
Under strongly stable conditions in winter (Floes 1 and 2), the estimated ABL height during N-ICE2015 rarely exceeds 100 m (Figure 8). The stable layer can extend up to 1500 m in the vertical, accompanied by an SBI with depth ranging from 600 to 1400 m. Above this layer the atmosphere mostly has neutral stability. Strong SBIs are associated with downward sensible heat flux, suppress mixing, and thereby limit the vertical extent of the ABL [*Walden et al.*, 2017]. Under such conditions the changes in ABL height result from dynamic influences, e.g., wind.

Cyclones affect both the dynamic and static stability of the atmosphere. First, the strong winds associated with cyclones have a large dynamic influence that manifests as sudden increases in ABL height. The maximum ABL height calculated during a cyclone event is about 1600 m (Figure 8). Cyclones also transport warm and moist air into the Arctic, which alters the static stability of the troposphere. Hence, the more heat and moisture a winter cyclone transports into the Arctic, the greater and longer is its impact on the static stability throughout the vertical column (Figure 8). For example, the sudden drop in ABL height and the change from neutral to unstable static stability during storm M2, coincides with the change in wind direction and passage of the cold front (Figures 3–6 and 8). Overall, the largest impact on tropospheric stability during the N-ICE2015 winter was due to cyclonic events, similar to the findings of *Kim et al.* [2017] for winter 2016 in this region.

Typical stability conditions for the winter are shown in Figure 9a: via the frequency distribution of the vertical gradient of virtual potential temperature. Further, Table 1 provides a summary of the results from Figures 9a and 9e for specific altitude ranges. The N-ICE2015 winter period exhibits stable stratification often due to the strong SBIs and near-surface LIs (Figures 8 and 9a). The most stable region is below 300 m. However,

Figure 8. Time-height cross section of static stability calculated from virtual potential temperature obtained from N-ICE2015 radiosonde data (color coded). Depicted are also the corresponding boundary layer height (solid black line) obtained from Richardson number $\left(Ri_{\mathrm{crit}} = 0.25\right)$ and the top height of the surface-based temperature inversion (white filled circles), when present, or of the lowest lifted inversion (magenta circles). Major (M1 to M8) and minor storm events are highlighted at the bottom (magenta and cyan lines in bottom subfigure, respectively).

Figure 9. Distributions, as a function of height, of the vertical potential temperature gradient from radiosondes (top row) during the winter months January-February-March and (bottom row) during the spring months April-May-June, (a and e) for the N-ICE2015 expedition, (c and g) for the ERA-Interim reanalysis profiles (January to June 2015) closest to R/V *Lance*'s location [*Dee et al.*, 2011], (c and g) for the SHEBA expedition, and (d and h) for Ny-Ålesund, respectively. The sum in each height bin (width = 25 m) is 100%.

Table 1. Static Stability Statistics[a]

Season	Range (km)	Strongly Stable (%) $0.03\ Km^{-1} \leq \partial_z \Theta_v)$	Stable (%) $0.01 \leq \partial_z \Theta_v < 0.03\ Km^{-1}$	Neutral (%) $0 \leq \partial_z \Theta_v < 0.01\ Km^{-1}$	Unstable (%) $\partial_z \Theta_v < 0\ Km^{-1}$
Winter	$0 < z \leq 0.3$	23	34	36	7
	$0.3 < z \leq 1$	5	41	50	4
	$1 < z \leq 3$	0	10	86	4
	$3 < z \leq 10$	0	14	80	6
Spring	$0 < z \leq 0.3$	4	13	51	32
	$0.3 < z \leq 1$	5	29	60	6
	$1 < z \leq 3$	1	11	84	4
	$3 < z \leq 10$	2	22	70	5

[a]Summarized from Figure 9.

locally unstable conditions are occasionally observed below 150 m. Neutral and stable conditions are abundant below 1000 m (Figure 9 and Table 1). Above 1000 m, the atmosphere becomes mostly neutral with increasing height.

3.4.2. Spring

Under polar day conditions during N-ICE2015 (Floes 3 and 4), the frequency of occurrence of SBIs is drastically reduced (to ∼7%). This decreases the depth and ΔT of LIs (Figures 7e and 7f). The frequency of occurrence of LIs remains high, ∼90% in all spring soundings. The distribution of LI base temperature is still bimodal, but the maximum frequency of occurrence has shifted toward higher temperatures (Figure 7g).

Dividing the spring period roughly before and after the onset of temperatures above 0°C enables a closer look at the inversion base temperature distribution (Figure 7g, green and black lines). Here we choose 24 May to include the soundings with lower tropospheric temperatures exceeding 0°C. This corresponds to the drift periods closer to the ice edge and over warmer waters [*Meyer et al.*, 2017] (Figures 1 and 2). The peak frequency of occurrence of inversion base temperature for LIs during these two separate periods coincides with the peaks of the entire spring observations (Figure 7g). The bimodality during spring (Floes 3 and 4) therefore should not be interpreted as the clear and opaque states in winter, but considered with respect to the meteorologic conditions gradually changing to summer conditions and to the ship's proximity to the ice edge.

The frequency of occurrence of SIs remains almost unchanged from winter (∼50% of all spring soundings). However, there is a shift in the monomodal distribution of the base temperatures and a greater frequency of occurrence of larger ΔT. Most often, the base of LIs is observed below 500 m with highest occurrence of ∼22% between 300 and 500 m (Figure 7h). The distributions of depth and base height highlight that there are only few SIs with bases below 600 m and that SIs are distributed evenly throughout altitudes ranging from 800 to 1700 m (Figures 7e and 7h).

During spring, the ABL height is more variable than in winter but with smaller vertical extent, not reaching beyond 1000 m (Figure 8). The stability in the ABL is largest in the presence of SBIs. The overall high occurrence of unstable static conditions in the boundary layer is an indication of turbulent mixing initiated by surface fluxes, caused by radiative heating of the surface [*Walden et al.*, 2017]. In the free troposphere, stable conditions occur below the LI top, whose base during spring is often found near the estimated ABL height (not shown). After the onset of snow melt (as estimated by near-surface temperatures remaining near 0°C), the LI depth and the extent of the stable layer above the LIs become smaller. The meteorological overview given by *Cohen et al.* [2017] suggests that most of the LIs during spring and early summer are associated with cloud top inversions.

During the N-ICE2015 spring period, a LI was present over the sea ice for most of the time with a base near the boundary layer height (Figure 7). Figure 9e, we observe an unstable to neutral region below about 150 m and a neutral to stable region from about 200 m to 1000 m (Figure 9d). Stability in spring is generally weaker than in winter (Figure 9a and Table 1). Neutral stratification is most frequent in the lowest 500 m. Above 1000 m, local stability is similar to the winter period. However, weakly stable conditions occur more frequently between 1000 and 2000 m during spring, due to the presence of LIs.

The change in local stability over sea ice from winter to spring, during N-ICE2015, is greatest near the surface (Figures 9a and 9e). The difference between the two shows the influence of turbulent surface fluxes driven by shortwave radiation flux on local static stability up to 300 m. Furthermore, the presence of LIs near the ABL top along with statically neutral to stable conditions indicates the presence of clouds [*Sedlar et al.*, 2012].

4. Comparison With ERA-Interim, SHEBA, and Ny-Ålesund

4.1. Static Stability Distributions

Here we compare the seasonal stability distribution from N-ICE2015 to ERA-Interim reanalysis [*Dee et al.*, 2011], SHEBA [*Moritz*, 2007], and Ny-Ålesund. SHEBA provides a similar data set to N-ICE2015 that covers winter and spring 1998, but took place farther into the ice pack and over thicker sea ice in the Beaufort Sea [*Uttal et al.*, 2002]. In contrast, the nearby land-based Ny-Ålesund station covers the same period as N-ICE2015 and is situated close to the N-ICE2015 site, but in a mountainous and ice-free fjord environment.
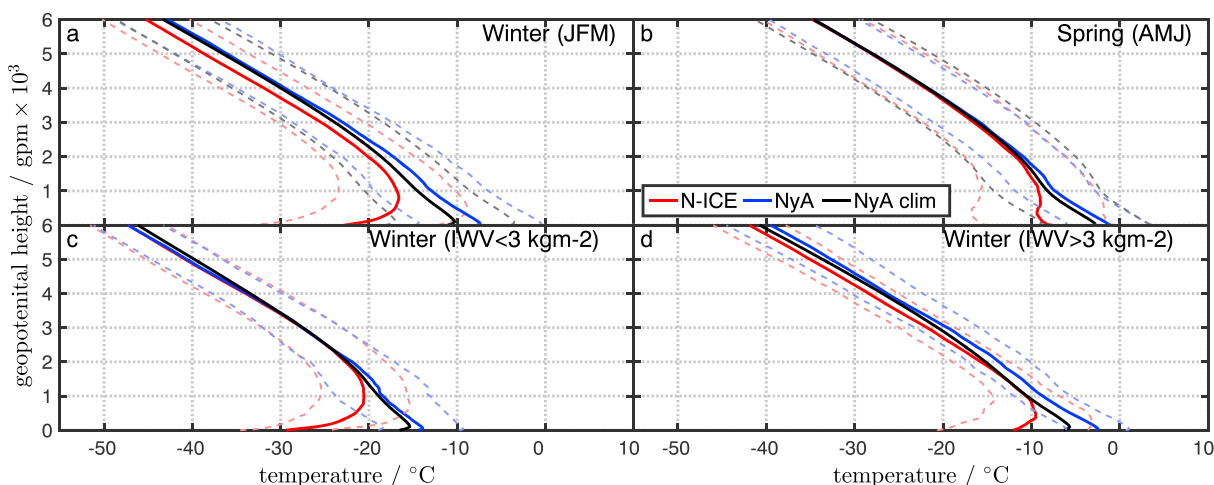
First, we compare stability distributions for N-ICE2015 and for ERA-Interim profiles, corresponding to the sea ice-covered grid point closest to R/V *Lance*'s positions. The reanalysis captures the general features of winter and spring well, but misses the strongly stable cases (Figures 9b and 9f). This comparison demonstrates that overall the reanalysis displays the general thermodynamic structure well. However, the reanalysis underestimates the strength and depth of temperature inversion in winter and in spring, despite the assimilation [*Tjernström and Graversen*, 2009; *Liu et al.*, 2015; *Graham et al.*, 2017]. In winter, the problems may be related to turbulent surface fluxes, while in spring, the stable inversion layers created by clouds seem to be underestimated.

We find similar stability characteristics for both N-ICE2015 and SHEBA. However, there are some differences. Interestingly, SHEBA has a higher frequency of occurrence for unstable conditions at both low and high altitudes in winter and spring. In contrast, N-ICE2015 displays a tendency toward more neutral conditions. The altitude range of the strongest stability reaches higher in SHEBA, up to 500 m. This is indicative of higher inversion tops during the SHEBA winter. But the differences occur in a region of the distribution with very few sample points and are likely not statistically significant. Above 600 m, differences between N-ICE2015 and SHEBA are relatively small for both seasons. For both campaigns we find a reduced occurrence of strongly stable conditions in the spring soundings, compared with the winter.

During the N-ICE2015 period, January to June 2015, in Ny-Ålesund, the atmospheric conditions were mostly neutral with shallower inversions in winter compared with N-ICE2015 (Figures 9c and 10a). The stable layer extends only to ~100 m at Ny-Ålesund compared with ~1000 m during N-ICE2015 and SHEBA. In winter, the frequency and range of occurrence of unstable conditions is comparable for Ny-Ålesund and for N-ICE2015. During the spring period, unstable conditions in the lowest 100 m are more frequent for Ny-Ålesund than for N-ICE2015. During both seasons, the virtual potential temperature gradient up to 1000 m at Ny-Ålesund is most frequently near $0\,\mathrm{K\,m^{-1}}$. This indicates that a well-mixed layer is present. Above 2000 m, the atmospheric stability for Ny-Ålesund is very similar to N-ICE2015. The atmospheric stability in the middle and upper troposphere for the campaign period over both locations are characteristic of the large-scale conditions in the Arctic region.

Overall, the boundary layer at Ny-Ålesund is more neutral compared to the sea ice environment during N-ICE2015 and SHEBA. At Ny-Ålesund, the atmospheric stability within the lowermost kilometer of the atmosphere is affected by the underlying surface (i.e., snow and open water) as well as dynamical effects induced by the surrounding orography. Both of these factors act to enhance mixing and reduce stability. Therefore, radiative cooling is less effective, resulting in a weaker and less frequent SBIs.

The comparison of static stability (Figure 9) during SHEBA and N-ICE2015 reveals that the N-ICE2015 observations over thinner, younger sea ice in the North Atlantic Arctic sector share similar tropospheric characteristics in the troposphere compared with other ice-covered regions and different ice regimes in the Arctic. Hence, on seasonal time scales, the influence of a thinner sea ice cover on the thermodynamic structure of the Arctic troposphere is weak compared to the impact of synoptic cyclones. Nonetheless, the N-ICE2015 campaign was characterized by an unusually thick snow cover that may have acted to insulate the atmosphere from the warm ocean [*Merkouriadi et al.*, 2017]. The comparison of N-ICE2015 and Ny-Ålesund observations reveals similar Arctic stability features in the free troposphere. However, the boundary layer stability and dynamics are clearly different over sea ice and the snow-covered, mountainous, and open ocean landscape.

Figure 10. Seasonal mean temperature profiles and standard deviation from the mean for (a) winter (JFM) and (b) spring (AMJ) for N-ICE2015 (red), Ny-Ålesund 2015 (blue), the Ny-Ålesund long-term (1993 to 2014) data set (black), respectively. For the winter season, mean profiles are shown with (c) low and (d) high IWV.

4.2. Temporal Placement

Figures 9 and 10 show that the free tropospheric temperatures and potential temperature gradients at N-ICE2015 and Ny-Ålesund are comparable above 2000 m. However, there is a constant offset between the mean winter N-ICE2015 and the corresponding Ny-Ålesund profile, with the N-ICE2015 profile being ~2.5°C colder than Ny-Ålesund. During winter both sites were affected by the same synoptic cyclones (section 3.3, Figures 4–6) This temperature offset occurs mainly in periods with high IWV, corresponding to the times of warm air advection from lower latitudes (Figures 10c and 10d). Using soundings from coinciding IWV increases greater than 3 kg m^{-2} reduces the offset to less than 1°C (not shown). This suggests that N-ICE2015 and Ny-Ålesund observe the synoptic events in different stages of their development and at different positions relative to their low-pressure centers (Figure 6). During periods of low IWV the profiles of both sites are comparable above 2000 m. The close proximity of N-ICE2015 and Ny-Ålesund, together with the similarities of the two campaign mean profiles above 2000 m for spring and summer, suggests that by comparing the 2015 Ny-Ålesund observations with the Ny-Ålesund climatology (1993–2014), we can place both Ny-Ålesund 2015 and the N-ICE2015 expedition campaign into a climatological context.

The winter 2015 Ny-Ålesund profiles are generally warmer compared to the 22 year climatology, up to an altitude of 4000 m height (Figure 10a). By considering only low IWV cases, the Ny-Ålesund 2015 winter mean profile is only slightly warmer in the lowest 2000 m and colder above 4000 m. For temperature profiles with IWV above 3 kg m^{-2}, the Ny-Ålesund 2015 winter mean profile is consistently warmer than the climatology (Figure 10d). This demonstrates the effect of cyclonic events on the winter mean temperatures at Ny-Ålesund. Overall, winter temperatures in the lowermost 250 m were up to 3°C warmer than the climatological mean (Figure 10a). Consistent with Arctic amplification being strongest in the lowermost troposphere [*Screen and Simmonds*, 2010], the difference of the 2015 Ny-Ålesund profiles to the climatological mean decreases with increasing altitude, reaching approximately 2°C at 2000 m and 1°C at 3000 m. This suggests that Ny-Ålesund, in particular, and also the Arctic North Atlantic sector are sensitive to events of warm and moist air advection from lower latitudes [*Woods and Caballero*, 2016; *Maturilli and Kayser*, 2016]. Using ERA-Interim reanalysis, *Graham et al.* [2017] show a positive trend in 2 m temperature and IWV for the Arctic North Atlantic sector. These trends correlate with a marked decrease in the number of clear days over the N-ICE2015 region, but only a small decrease West of Svalbard, close to Ny-Ålesund. [*Graham et al.*, 2017, Figures 7 and 8]. Therefore, a smaller number of clear days likely adds to the long-term warming trend in the Arctic North Atlantic sector, including the N-ICE2015 region and Ny-Ålesund [*Graham et al.*, 2017].

In accordance with greater Arctic warming trends in winter, the temperature difference between 2015 and the climatology at Ny-Ålesund is less in spring than in winter (Figure 10). In spring 2015, Ny-Ålesund was only 2°C warmer near the surface, compared with the climatology, and less than 0.5°C warmer at 2000 m. The 2015 mean spring profile Ny-Ålesund is practically indistinguishable from the climatology in the free troposphere, and the mean N-ICE2015 profile for spring closely matches the Ny-Ålesund climatology above 2000 m.

Synoptic systems observed during the N-ICE2015 spring were mostly located toward the east in the Barents and Kara Seas, rather than tracking northward from the Atlantic to pass over Ny-Ålesund then N-ICE2015 (section 3.3) [*Cohen et al.* [2017, Figure 6d]. As a result, N-ICE2015 does not show the signal of weakened temperature advection compared with Ny-Ålesund that was observed during winter. Overall, the spring mean profiles of 2015 for both sites indicate that this season was typical for the Arctic North Atlantic sector, of the Arctic, when compared to long-term radiosonde observations at Ny-Ålesund. This is consistent with the findings of *Cohen et al.* [2017] using the NCEP-NCAR reanalysis.

5. Summary and Conclusions

The radiosonde observations of N-ICE2015 from January to June 2015 present a new data set in the otherwise data-sparse Arctic region north of Svalbard. These observations are especially valuable, because they cover winter, spring, and early summer conditions over the younger, thinner sea ice regime in the Arctic North Atlantic sector. Here we analyze the radiosonde profiles and provide detailed characteristics of cyclonic events in terms of vertical thermodynamic structure; rapid increases in IWV and temperature; temperature inversions; and boundary layer height.

These cyclonic events or Arctic storms influence the temperatures and moisture content of the atmospheric boundary layer and the lowermost troposphere more than in the upper troposphere. However, temperature increases throughout the entire tropospheric column are observed, together with sudden increases in IWV. The impact of storms is most visible during winter, when radiative cooling of the surface is most effective and the background moisture is low (<3 kg m^{-2}). During spring and early summer (AMJ, April-May-June), the synoptic cyclones observed during N-ICE2015 were centered over the Barents and Kara Seas, and their impact at the N-ICE2015 position was smaller compared with winter, when systems passed directly overhead (Figure 4) [*Cohen et al.*, 2017, Figures 9 and 10]. During spring and early summer, the background moisture content gradually increases due to the seasonal cycle, but peaks in moisture content continue to coincide with warm air advection. IWV is therefore a useful indicator of advected air masses in the Arctic.

Analyses of basic temperature inversion characteristics during N-ICE2015 reveals that with SBIs occurred in 58% of all winter soundings (Figure 7). An inversion was found below 500 m (in 94% of all soundings). In the winter period, statically unstable conditions are only observed during synoptic events. The absent or negligible shortwave radiation during JFM allows for strong radiative cooling and creates deep SBIs.

In contrast with winter, SBIs are rare in spring. However, LIs are still found in 90% of all soundings. Under polar day conditions, surface fluxes lift the temperature inversions base to greater altitudes and thereby restrict the depth and strength of LIs. The ABL was frequently unstable, and the ABL height was more variable during spring compared with winter. In spring, characteristics of SIs change little from those in winter. SIs occur in ~50% of all soundings.

We show that the static stability throughout the troposphere for N-ICE2015 closely resembles earlier observations from SHEBA during winter and spring, despite the two campaigns taking place in different regions of the Arctic with different ice and synoptic regimes (Figure 9). In particular, the frequency distribution, as a function of height, of locally stable, neutral, and unstable regions are similar, despite the two campaigns taking place in different regions of the Arctic with different ice and synoptic regimes. This suggests that on seasonal time scales a thinner sea ice cover, which is insulated by a thick snow cover, has little influence on the thermodynamic structure of the Arctic troposphere compared to synoptic cyclones entering the Arctic.

We further compare the static stability of N-ICE2015 to the nearby land-based measurement site, Ny-Ålesund. In contrast with the sea ice environment at N-ICE2015, Ny-Ålesund is characterized by snow-covered mountains and an ice-free fjord. The two sites display similar vertical profiles for both winter and spring throughout the free troposphere above 2000 m (Figure 10). However, in the boundary layer the profiles are very different. The boundary layer at Ny-Ålesund is more frequently neutral and warmer compared with sea ice-covered regions.

The close proximity of N-ICE2015 and Ny-Ålesund and the similarities between the upper air profiles from these two observation sites, allow us to use the long-term record from Ny-Ålesund to place N-ICE2015 into a climatological context. Consistent with the findings from *Cohen et al.* [2017], we find that the Ny-Ålesund

2015 winter was warmer than the long-term mean, while the spring period was close to the climatological mean. Clustering of the winter temperature profiles in high and low IWV events demonstrates the importance of cyclonic events for the winter mean temperatures at Ny-Ålesund, especially in the lowermost 3000 m.

Generally, studies of Arctic storms show that the most insight is gained from multiinstrument approaches using in situ data, satellite observations and reanalysis [*Persson et al.*, 2016]. However, most synoptic cyclones are not observed in situ [*Kim et al.*, 2017]. This makes the complete meteorological observations obtained during the N-ICE2015 expedition [*Graham et al.*, 2017; *Cohen et al.*, 2017; *Walden et al.*, 2017], including cloud data and surface radiation especially valuable. Focusing on the boundary layer characteristics, the metrics presented in our study can be used to evaluate regional climate models. Those will help to improve parameterizations and process understanding, which in return can be implemented in larger-scale climate models and in climate reanalysis.

References

Andreas, E. L., K. J. Claffy, and A. P. Makshtas (2000), Low-level atmospheric jets and inversions over the Western Weddell Sea, *Boundary Layer Meteorol.*, *97*(3), 459–486, doi:10.1023/A:1002793831076.

Andreas, E. L., P. O. G. Persson, A. A. Grachev, R. E. Jordan, T. W. Horst, P. S. Guest, and C. W. Fairall (2010), Parameterizing turbulent exchange over sea ice in winter, *J. Hydrometeorol.*, *11*(1), 87–104, doi:10.1175/2009JHM1102.1.

Bekryaev, R. V., I. V. Polyakov, and V. A. Alexeev (2010), Role of polar amplification in long-term surface air temperature variations and modern arctic warming, *J. Clim.*, *23*(14), 3888–3906, doi:10.1175/2010JCLI3297.1.

Cohen, L., S. R. Hudson, V. P. Walden, R. M. Graham, and M. A. Granskog (2017), Meteorological conditions in a thinner Arctic sea ice regime from winter through summer during the Norwegian young sea ICE expedition (N-ICE2015), *J. Geophys. Res. Atmos.*, *122*, doi:10.1002/2016JD026034, in press.

Comiso, J. C., and D. K. Hall (2014), Climate trends in the Arctic as observed from space, *WIREs Clim. Change*, *5*(3), 389–409, doi:10.1002/wcc.277.

Dee, D. P., et al. (2011), The ERA-Interim reanalysis: Configuration and performance of the data assimilation system, *Q. J. R. Meteorol. Soc.*, *137*(656), 553–597, doi:10.1002/qj.828.

Dirksen, R. J., M. Sommer, F. J. Immler, D. F. Hurst, R. Kivi, and H. Vömel (2014), Reference quality upper-air measurements: GRUAN data processing for the Vaisala RS92 radiosonde, *Atmos. Meas. Tech.*, *7*(12), 4463–4490, doi:10.5194/amt-7-4463-2014.

Engström, A., J. Karlsson, and G. Svensson (2014), The importance of representing mixed-phase clouds for simulating distinctive atmospheric states in the Arctic, *J. Clim.*, *27*(1), 265–272, doi:10.1175/JCLI-D-13-00271.1.

Grachev, A. A., E. L. Andreas, C. W. Fairall, P. S. Guest, and P. O. G. Persson (2007), Sheba flux-profile relationships in the stable atmospheric boundary layer, *Boundary Layer Meteorol.*, *124*(3), 315–333, doi:10.1007/s10546-007-9177-6.

Graham, R., A. Rinke, L. Cohen, S. R. Hudson, V. P. Walden, M. A. Granskog, W. Dorn, M. Kayser, and M. Maturilli (2017), A comparison of the two Arctic atmospheric winter states observed during N-ICE2015 and SHEBA, *J. Geophys. Res. Atmos.*, *122*, 5716–5737, doi:10.1002/2016JD025475.

Granskog, M. A., P. Assmy, S. Gerland, G. Spreen, H. Steen, and L. H. Smedsrud (2016), Arctic research on thin ice: Consequences of Arctic sea ice loss, *Eos Trans. AGU*, *97*, 22–26, doi:10.1029/2016EO044097.

Graversen, R. G., and M. Wang (2009), Polar amplification in a coupled climate model with locked albedo, *Clim. Dyn.*, *33*(5), 629–643, doi:10.1007/s00382-009-0535-6.

Gryning, S.-E., and E. Batchvarova (2002), Marine boundary layer and turbulent fluxes over the baltic sea: Measurements and modelling, *Boundary Layer Meteorol.*, *103*(1), 29–47, doi:10.1023/A:1014514513936.

Hanna, S. R. (1969), The thickness of the planetary boundary layer, *Atmos. Environ.*, *3*, 519–536, doi:10.1016/0004-6981(69)90042-0.

Hudson, S., L. Cohen, M. Kayser, M. Maturilli, J. Kim, S. J. Park, W. Moon, and M. A. Granskog (2017), *N-ICE2015 Atmospheric Profiles From Radiosondes*, Norwegian Polar Institute, Alfred Wegener Institute, Korean Polar Research Institute [Dataset], doi:10.21334/npolar.2017.216df9b3. [Available at https://data.npolar.no/dataset/216df9b3-e2bd-5111-9c02-fea848d76670.]

Hudson, S. R., L. Cohen, and V. Walden (2015), N-ICE2015 surface meteorology [Data set], Norwegian Polar Inst., Tromsø, doi:10.21334/npolar.2015.056a61d1, Accessed 14 June 2016.

Itkin, P., G. Spreen, B. Cheng, M. Doble, F. Girard-Ardhuin, J. Haapala, N. Hughes, L. Kaleschke, M. Nicolaus, and J. Wilkinson (2017), Thin ice and storms: Sea ice deformation from buoy arrays deployed during N-ICE2015, *J. Geophys. Res. Oceans*, *122*(6), 4661–4674, doi:10.1002/2016JC012403.

Kim, B.-M., J.-Y. Hong, S.-Y. Jun, X. Zhang, H. Kwon, S.-J. Kim, J.-H. Kim, S.-W. Kim, and H.-K. Kim (2017), Major cause of unprecedented Arctic warming in January 2016: Critical role of an Atlantic windstorm, *Sci. Rep.*, *7*, 40051, doi:10.1038/srep40051.

Liu, Z., A. Schweiger, and R. Lindsay (2015), Observations and modeling of atmospheric profiles in the Arctic seasonal ice zone, *Mon. Weather Rev.*, *143*(1), 39–53, doi:10.1175/MWR-D-14-00118.1.

Lüpkes, C., and V. M. Gryanik (2015), A stability-dependent parametrization of transfer coefficients for momentum and heat over polar sea ice to be used in climate models, *J. Geophys. Res. Atmos.*, *120*, 552–581, doi:10.1002/2014JD022418.

Maturilli, M., and M. Kayser (2016), Arctic warming, moisture increase and circulation changes observed in the Ny-Ålesund homogenized radiosonde record, *Theor. Appl. Climatol.*, 1–17, doi:10.1007/s00704-016-1864-0.

Merkouriadi, I., J.-C. Gallet, G. E. Liston, C. Polashenski, R. M. Graham, A. Rösel, and S. Gerland (2017), Winter snow conditions on Arctic sea ice north of Svalbard during the Norwegian young sea ICE (N-ICE2015) expedition, *J. Geophys. Res. Atmos.*, *122*, doi:10.1002/2016JD026753, in press.

Meyer, A., et al. (2017), Winter to summer oceanographic observations in the Arctic Ocean north of Svalbard, *J. Geophys. Res. Oceans*, doi:10.1002/2016JC012391.

Miloshevich, L. M., H. Vömel, A. Paukkunen, A. J. Heymsfield, and S. J. Oltmans (2001), Characterization and correction of relative humidity measurements from Vaisala RS80-A radiosondes at cold temperatures, *J. Atmos. Oceanic Technol.*, *18*(2), 135–156, doi:10.1175/1520-0426(2001)018<0135:CACORH>2.0.CO;2.

Moritz, R. E. (2007), Soundings, Ice Camp NCAR/GLAS raobs. (ASCII). Version 2.0 (Version 2.0) [Data set], UCAR/NCAR - Earth Observing Laboratory, doi:10.5065/d6fq9v0z.

Persson, P. O. G., M. D. Shupe, D. Perovich, and A. Solomon (2016), Linking atmospheric synoptic transport, cloud phase, surface energy fluxes, and sea-ice growth: Observations of midwinter Sheba conditions, *Clim. Dyn.*,1–24, doi:10.1007/s00382-016-3383-1.

Pithan, F., and T. Mauritsen (2014), Arctic amplification dominated by temperature feedbacks in contemporary climate models, *Nat. Geosci.*, *7*(3), 181–184, doi:10.1038/ngeo2071.

Pithan, F., et al. (2016), Select strengths and biases of models in representing the Arctic winter boundary layer over sea ice: The Larcform 1 single column model intercomparison, *J. Adv. Model. Earth Syst.*, *8*, 1345–1357, doi:10.1002/2016MS000630.

Rinke, A., P. Marbaix, and K. Dethloff (2004), Internal variability in Arctic regional climate simulations: Case study for the SHEBA year, *Clim. Res.*, *27*(3), 197–209, doi:10.3354/cr027197.

Screen, J. A., and I. Simmonds (2010), The central role of diminishing sea ice in recent Arctic temperature amplification, *Nature*, *464*(7293), 1334–1337, doi:10.1038/nature09051.

Sedlar, J., M. D. Shupe, and M. Tjernström (2012), On the relationship between thermodynamic structure and cloud top, and its climate significance in the Arctic, *J. Clim.*, *25*(7), 2374–2393, doi:10.1175/JCLI-D-11-00186.1.

Serreze, M. C., and R. G. Barry (1988), Synoptic activity in the Arctic basin, 1979–85, *J. Clim.*, *1*(12), 1276–1295, doi:10.1175/1520-0442(1988)001<1276:SAITAB>2.0.CO;2.

Serreze, M. C., F. Carse, R. G. Barry, and J. C. Rogers (1997), Icelandic low cyclone activity: Climatological features, linkages with the NAO, and relationships with recent changes in the Northern Hemisphere circulation, *J. Clim.*, *10*(3), 453–464, doi:10.1175/1520-0442(1997)010<0453:ILCACF>2.0.CO;2.

Shupe, M. D., S. Y. Matrosov, and T. Uttal (2006), Arctic mixed-phase cloud properties derived from surface-based sensors at Sheba, *J. Atmos. Sci.*, *63*(2), 697–711, doi:10.1175/JAS3659.1.

Sommer, M., R. Dirksen, and F. Immler (2012), *RS92 GRUAN Data Product Version 2 (RS92-GDP.2)*, GRUAN Lead Centre, Lindenberg, doi:10.5676/GRUAN/RS92-GDP.2.

Steinbrecht, W., H. Claude, F. Schönenborn, U. Leiterer, H. Dier, and E. Lanzinger (2008), Pressure and temperature differences between Vaisala RS80 and RS92 radiosonde systems, *J. Atmos. Oceanic Technol.*, *25*(6), 909–927, doi:10.1175/2007JTECHA999.1.

Stramler, K., A. D. D. Genio, and W. B. Rossow (2011), Synoptically driven Arctic winter states, *J. Clim.*, *24*(6), 1747–1762, doi:10.1175/2010JCLI3817.1.

Stull, R. B. (1991), Static stability—An update, *Bull. Am. Meteorol. Soc.*, *72*(10), 1521–1529, doi:10.1175/1520-0477(1991)072<1521:SSU>2.0.CO;2.

Taylor, G. I. (1931), Effect of variation in density on the stability of superposed streams of fluid, *Proc. R. Soc. A*, *132*(820), 499–523.

Tjernström, M., and R. G. Graversen (2009), The vertical structure of the lower Arctic troposphere analysed from observations and the ERA-40 reanalysis, *Q. J. R. Meteor. Soc.*, *135*(639), 431–443, doi:10.1002/qj.380.

Uttal, T., et al. (2002), Surface heat budget of the Arctic Ocean, *Bull. Am. Meteorol. Soc.*, *83*(2), 255–275, doi:10.1175/1520-0477(2002)083<0255:SHBOTA>2.3.CO;2.

Walden, V. P., S. R. Hudson, L. Cohen, S. Y. Murphy, and M. A. Granskog (2017), Atmospheric components of the surface energy budget over young sea ice: Results from the N-ICE2015 campaign, *J. Geophys. Res. Atmos.*, doi:10.1002/2016JD026091, in press.

Wallace, J. M., and P. V. Hobbs (2006), *Atmospheric Science: An Introductory Survey*, pp. 375–417, vol. 92, Academic Press, New York.

Wang, X., J. Key, Y. Liu, C. Fowler, J. Maslanik, and M. Tschudi (2012), Arctic climate variability and trends from satellite observations, *Adv. Meteorol.*, *2012*, 505613, doi:10.1155/2012/505613.

Woods, C., and R. Caballero (2016), The role of moist intrusions in winter Arctic warming and sea ice decline, *J. Clim.*, *29*(12), 4473–4485, doi:10.1175/JCLI-D-15-0773.1.

Zhang, Y., Z. Gao, D. Li, Y. Li, N. Zhang, X. Zhao, and J. Chen (2014), On the computation of planetary boundary-layer height using the bulk Richardson number method, *Geosci. Model Dev.*, *7*(6), 2599–2611, doi:10.5194/gmd-7-2599-2014.

Zilitinkevich, S., and A. Baklanov (2002), Calculation of the height of the stable boundary layer in practical applications, *Boundary Layer Meteorol.*, *105*(3), 389–409, doi:10.1023/A:1020376832738.